ARTICLE

Check for updates

Dependency of solvation effects on metal identity in surface reactions

Mehdi Zare[1], Mohammad Saleheen[1], Subrata Kumar Kundu[1] & Andreas Heyden [1✉]

Solvent interactions with adsorbed moieties involved in surface reactions are often believed to be similar for different metal surfaces. However, solvents alter the electronic structures of surface atoms, which in turn affects their interaction with adsorbed moieties. To reveal the importance of metal identity on aqueous solvent effects in heterogeneous catalysis, we studied solvent effects on the activation free energies of the O–H and C–H bond cleavages of ethylene glycol over the (111) facet of six transition metals (Ni, Pd, Pt, Cu, Ag, Au) using an explicit solvation approach based on a hybrid quantum mechanical/molecular mechanical (QM/MM) description of the potential energy surface. A significant metal dependence on aqueous solvation effects was observed that suggests solvation effects must be studied in detail for every reaction system. The main reason for this dependence could be traced back to a different amount of charge-transfer between the adsorbed moieties and metals in the reactant and transition states for the different metal surfaces.

[1] Department of Chemical Engineering, University of South Carolina, 301 Main Street, Columbia, South Carolina 29208, USA. ✉email: heyden@cec.sc.edu

The widespread use of solvents in applications varying from pharmaceutical[1–6] to electrochemistry[7–10] and catalysis[11–16] has given rise to an extensive range of studies aimed at understanding and predicting the role of solvents. The concept that a solvent can alter the performance of a catalyst, including its rate, selectivity, and stability, is well known; yet predicting a specific solvation effect remains a challenge[17–24]. While impressive progress has been made in understanding the effects of solvents in homogenous catalysis[25–29], for heterogeneously catalyzed processes that benefit from easier separation of the catalyst relative to homogeneously catalyzed processes[30], the role of solvents is hardly understood and only rarely studied. The inherent complexity of a reaction system containing both a complex heterogeneous catalyst and a condensed phase at a finite, often elevated, temperature has resulted in only few systematic experimental (in situ and in operando)[13,15,31,32] and/or theoretical studies[11,12,33,34] of solvation effects in heterogenous catalysis.

The role of solvents in catalytic transformations occurring at a solid-liquid interface is typically ascribed to: heightened importance of mass transfer effects, nature of solvent (polarity etc.)[35–37], competitive adsorption between solvent molecules and adsorbed moieties[32,38,39], direct participation of the solvent in the reaction coordinate[40], and/or relative stabilization of reactant, transition and/or product state of elementary reactions[41–43]. These effects in turn can lead to a change in reaction mechanism, reaction kinetics, selectivity, and overall catalyst lifetime. In short, understanding and predicting solvent effects on surface reactions requires detailed investigations of the direct and indirect interactions between the solvent, catalyst, and reacting moieties on the surface under reaction conditions.

In this regard, theoretical calculations have the advantage of being able to systemically study the effect of an individual parameter on the effect of a solvent. Ab initio molecular dynamics (AIMD) simulations have been used[44–46]; however, due to the great computational cost associated with the quantum mechanical calculations and the large amount of phase space sampling necessary, AIMD simulations are currently limited to simulation systems of a few hundred atoms and a time scale of tens or a few hundred picoseconds[10,47,48].

An alternative approach is to use implicit solvation models[49,50]. While they can compute free energies of reactions at solid-liquid interfaces rapidly, their reliability has often been questioned[14] because of their inability to capture the anisotropic site-specific interactions between the solute and the solvent molecules. A compromise in efficiency and accuracy constitutes a combined quantum mechanical/molecular mechanical (QM/MM) approach[51–53]. In this class of simulations, the adsorbate and metal atoms involved in the reaction are considered as a QM sub-system described from first principles, while the bulk of the solvent and metal atoms distant to the active site are considered as an MM sub-system described using classical molecular mechanics force fields. We have previously developed such a hybrid QM/MM model, named eSMS (explicit solvation model for metal surfaces)[54], which considers the long-range electrostatic interaction of the solvent molecules in the electronic structure calculation of the active site and applied it to the free energy calculation of the initial dehydrogenation and dehydroxylation of an adsorbed ethylene glycol (EG) moiety on Pt(111) in the presence of liquid water[55].

To design a liquid-phase surface-catalyzed reaction system for enhanced activity and selectivity, the interrelation of energetic changes on variation of catalyst surface, nature of solvent, and reacting moiety must be disclosed. In this context, several studies have been dedicated to understanding how the nature of the solvent and reacting moiety direct catalysis[23,26,56–58]. Nonetheless, the role of the metal identity (catalyst) on the solvent

effect has to our knowledge not been investigated yet. While it could be argued that solvation effects should be similar for the same bond cleavages or for the same adsorbates on different metal surfaces such as in recent studies by Greely et al.[59,60], we hypothesize that the electronic structure modification of the metal surface and reacting moiety as a result of the nearby solvent is sufficiently significant that solvation effects can differ significantly for different metals. To confirm this hypothesis, we have investigated the aqueous-phase effects on the initial C–H and O–H bond cleavages of EG over the (111) facet of six transition metal surfaces (Ni, Pd, Pt, Cu, Ag, Au) using our explicit solvation method, eSMS. The choice of reaction systems is motivated by (i) EG being a commonly studied surrogate molecule of biomass-derived polyols, (ii) the selected transition metals are relatively stable and commonly used for aqueous-phase processing of biomass-derived oxygenates[61], (iii) early dehydrogenation steps of EG over Pt and Ni/Pt catalysts have previously been found to control the overall reaction rate[62–64], (iv) at least over Pt(111) in the vapor phase, initial C–H and O–H bond cleavage are competitive (although O–H bond cleavage is believed to be somewhat favored)[34,64], and finally (v), explicit solvation approaches have recently been used to demonstrate that for bond cleavage reactions of alcohols over Pt(111), aqueous solvation effects are large and can currently not be described by implicit solvation models[55,65].

Results

Figure 1 illustrates the aqueous-phase effects on the activation free energy barrier of the O–H ($CH_2OHCH_2OH^{**} + ^* \leftrightarrow CH_2OCH_2OH^{**} + H^*$) and C–H bond cleavages ($CH_2OHCH_2OH^{**} + ^* \leftrightarrow CHOHCH_2OH^{**} + H^*$) of EG at 423 K computed by eSMS (see Table 1 for specific numbers). In addition, a graphical representation of the free-energy (potential of mean force) profiles for the O–H bond cleavages is illustrated in Fig. 2 and for the C–H bond cleavages in Supplementary Fig. 1. We note that although some of the metals (such as Ni) might get partially oxidized in liquid water environments with low reduction potential, we chose to study the (111) facet of all metal surfaces for better comparison. Generally, both O–H and C–H bond cleavages are somewhat facilitated in the presence of water. For the O–H bond cleavage, Pt is the most active catalyst in both phases. However, for the C–H bond cleavage, Ni is the most active catalyst in the presence of liquid water because of strong aqueous-phase effect that is more than twice as large over Ni than Pt. Interestingly, in liquid water Cu is predicted to be as active for
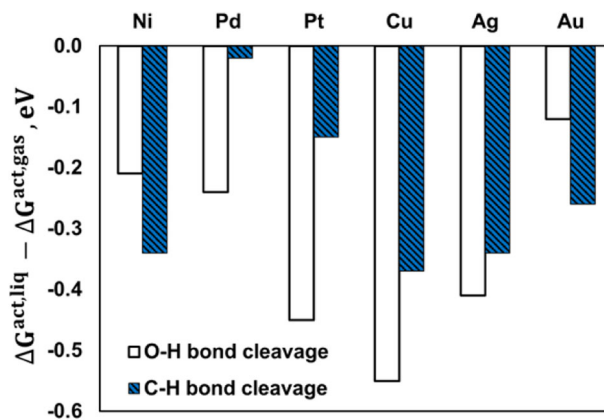
Fig. 1 Aqueous-phase effects on the activation free energy barriers by eSMS. The investigated reactions include the O–H and C–H bond cleavages of ethylene glycol over the (111) surface facet of six transition metals at 423 K (all structures optimized in liquid water; see Table 1 for specific numbers).

Table 1 Free energies of activation of O–H bond cleavage ($CH_2OHCH_2OH^{**} + ^* \leftrightarrow CH_2OCH_2OH^{**} + H^*$) and C–H bond cleavage ($CH_2OHCH_2OH^{**} + ^* \leftrightarrow CHOHCH_2OH^{**} + H^*$) of ethylene glycol in gas- and aqueous-phase environments over the (111) surface facet of six transition metals at 423 K.

Metal	Reaction Environment	O–H cleavage	C–H cleavage
Ni(111)	Vapor Phase	0.70	0.79
	VASPsol	0.67	0.73
	iSMS	0.62	0.75
	QM/MM-FEP	0.49 ± 0.06	0.45 ± 0.00
	QM/MM-MFEP-OPT	0.55 ± 0.06	0.43 ± 0.02
Pd(111)	Vapor Phase	0.83	0.76
	VASPsol	0.85	0.68
	iSMS	0.86	0.75
	QM/MM-FEP	0.59 ± 0.00	0.74 ± 0.02
	QM/MM-MFEP-OPT	0.58 ± 0.00	0.76 ± 0.02
Pt(111)	Vapor Phase	0.68	0.71
	VASPsol	0.82	0.64
	iSMS	0.62	0.62
	QM/MM-FEP	0.23 ± 0.01	0.56 ± 0.01
	QM/MM-MFEP-OPT	0.25 ± 0.01	0.55 ± 0.01
Cu(111)	Vapor Phase	1.08	1.43
	VASPsol	1.01	1.31
	iSMS	0.99	1.31
	QM/MM-FEP	0.52 ± 0.04	1.06 ± 0.00
	QM/MM-MFEP-OPT	0.50 ± 0.03	1.02 ± 0.00
Ag(111)	Vapor Phase	1.63	1.91
	VASPsol	1.65	1.81
	iSMS	1.57	1.88
	QM/MM-FEP	1.22 ± 0.04	1.57 ± 0.03
	QM/MM-MFEP-OPT	1.14 ± 0.04	1.56 ± 0.03
Au(111)	Vapor Phase	1.67	1.69
	VASPsol	1.75	1.43
	iSMS	1.64	1.52
	QM/MM-FEP	1.55 ± 0.00	1.43 ± 0.01
	QM/MM-MFEP-OPT	1.51 ± 0.01	1.41 ± 0.03

QM/MM-FEP indicates a free energy calculation in water between the critical points identified by gas-phase calculations (using the gas-phase vibrational partition function for the reactant and transition states). QM/MM-MFEP-OPT represents a free energy calculation in water for the different cleavages between the respective reactant and transition states that have been optimized in an aqueous-phase environment. Here, the vibrational partition functions are computed in the aqueous phase assuming the timescale for reorientation of the solvent molecules is much larger than the timescale for molecular vibrations. For comparison, implicit solvation calculations have also been performed using both nonperiodic (iSMS)[69] and periodic (VASPsol)[70,71] approaches. All numbers are in eV.

O–H bond cleavage ($\Delta G^{act,liq} = 0.50$ eV) as Ni ($\Delta G^{act,liq} = 0.55$ eV) and Pd ($\Delta G^{act,liq} = 0.58$ eV). In short, evidenced by very different aqueous-phase effects on the activation free energy barriers across different metals, our hypothesis that the nature of metal plays a key role for solvation effects on surface reactions has been confirmed.

Origin of dependency of solvent effect on metal identity. A heterogeneously catalyzed reaction occurring at a catalyst-solvent interface is at least a three-body problem involving solvent, catalyst, and reacting moiety. Thus, the most important factors contributing to solvation effects in such catalytic transformation arise from direct and indirect interactions of solvent, catalyst, and

reacting moiety. To explain the origin for the variability of aqueous-phase effects on the free energy of activation ($\Delta\Delta G^{act} = \Delta G^{act,liq} - \Delta G^{act,gas}$) of O–H and C–H bond cleavages of EG across six transition metals, we investigated some intuitive, physics-based descriptors.

One possible descriptor that could explain the role of the metal identity, which leads to different $\Delta\Delta G^{act}$ values across different metals and bond cleavages, is the difference in charge-transfer effects (and thus solvent stabilization) in the reactant (RS) and transition states (TS) (see Supplementary Table 5). This charge transfer effect is attributed to the indirect influence of the water environment causing an electronic modification of the metal atoms and the effective charge distribution in the reacting moieties. We note that, using AIMD simulations, Siemer et al.[17] have recently shown that water induced local charge transfer is a leading contribution for the observed solvation effect on O_2 activation at Au/TiO$_2$ interface sites. We choose two suitable descriptors for quantifying this charge-transfer effect. One is the cleaving-bond charge transfer (BC) defined as the change in sum of partial NPA[66] charges on the cleaving bond going from RS to TS; for example in O–H bond cleavage: $BC = |Q^H + Q^H|^{RS} - |Q^O + Q^H|^{TS}$. The idea behind this formula is that a change in charge from, e.g., -0.1 to $+0.1$, $+0.1$ to $+0.1$, or -0.1 to -0.1, should all result in no significant net stabilization since water stabilizes the RS and TS similarly. Another descriptor describing a charge-transfer effect is the molecular charge transfer (MC) defined here as the change in absolute sum of charges on the reacting moiety going from RS to TS, i.e., this descriptor describes the change in charge transfer from the metal surface to the reacting moiety when going from the RS to the TS.

Table 2 lists BC and MC for the O–H and C–H bond cleavages over the (111) facet of six transition metal surfaces (see Supplementary Table 5 for partial charges). According to our definition of BC and MC, smaller BC values (more negative) or larger MC values (more positive) correspond to an increased charge-transfer effect when going from reactant to transition state. For instance, in the C–H bond cleavage, the charge-transfer effect over Cu(111) ($BC = -0.46$ e, $MC = 0.53$ e) is higher than over Pt(111) ($BC = -0.03$ e, $MC = 0.08$ e). As shown in Table 2, $\Delta\Delta G^{act}$ is directly related to the charge-transfer effect descriptors in the C–H bond cleavage; that is, solvent effects increase (more negative $\Delta\Delta G^{act}$) with increasing charge-transfer effect (more negative BC or more positive MC). In contrast, for O–H bond cleavage, there is no linear relationship between $\Delta\Delta G^{act}$ and the charge-transfer effect. Nevertheless, after investigating other solvation effect descriptors, we will show that the charge-transfer effect is likely also here a key descriptor for the solvent effect across metal surfaces.

Another commonly used criterion for describing adsorbate-solvent interaction in an aqueous phase is hydrogen bonding[23,41]. Two main classes of hydrogen bonding definitions commonly used in the literature are based on an energy criterion and a geometric definition. Herein, we employed a geometric definition in which a hydrogen bond exists if the distance between the donor oxygen (O_d) and the acceptor oxygen (O_a), R_{OO}, is less than 3.2 Å and the angle $\angle HO_dO_a$ is smaller than 20°[67] (see Supplementary Fig. 2). We note that EG with OH functional groups can be either a donor or acceptor of hydrogen bonding (Supplementary Table 4). Hence, the change in mean of total hydrogen bonding (acceptor + donor) going from RS to TS was chosen as a descriptor, named in the following H-bond, and is included in Table 2. Next, the gas-phase free energy of activation ($\Delta G^{act,gas}$), a rough measure of change in surface-adsorbate interaction going from reactant to transition state was selected as a descriptor for describing the variability in solvation free energy
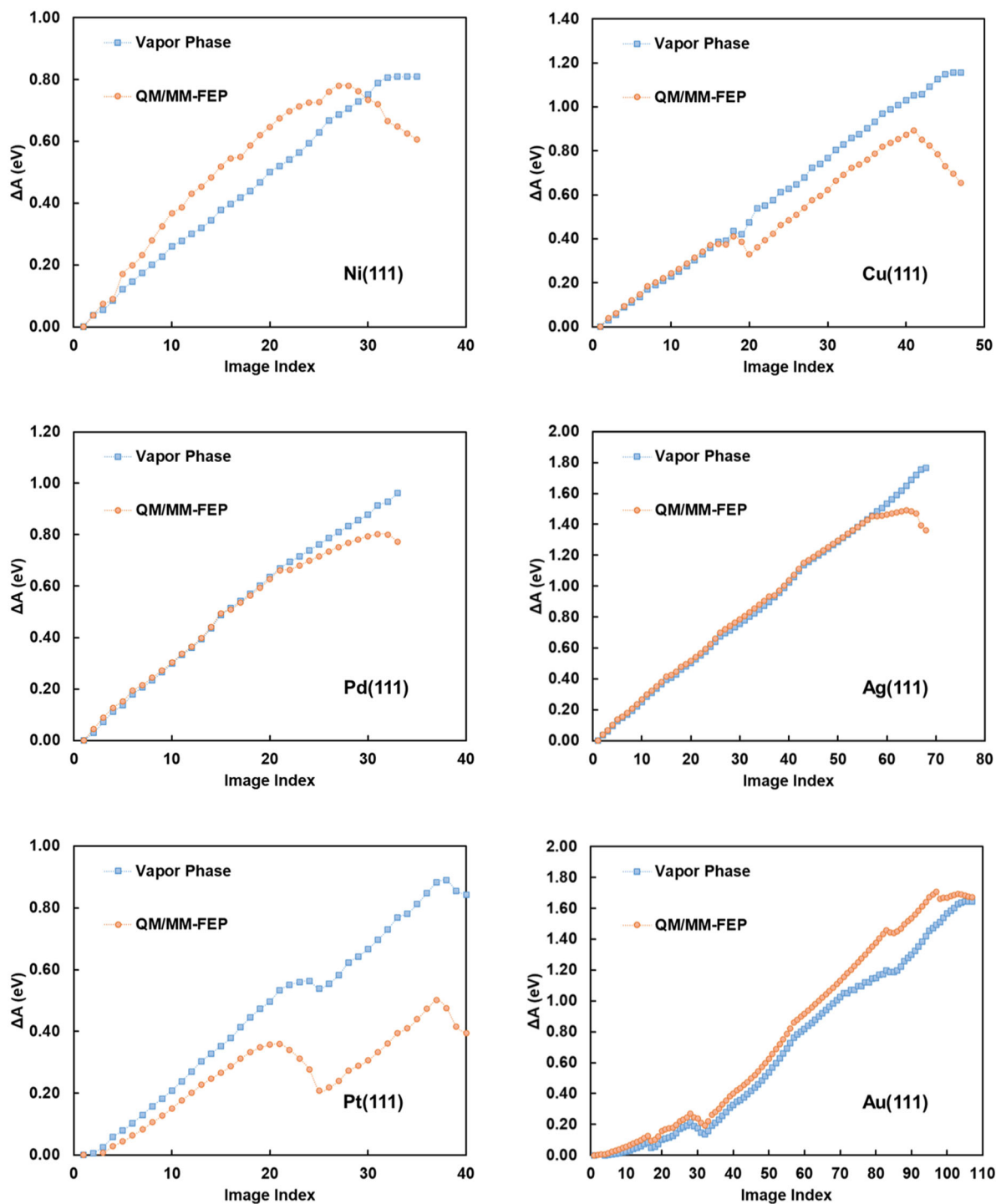
Fig. 2 Free-energy profiles for O–H bond cleavage of ethylene glycol at 423 K. The profiles are for vapor and aqueous phase over the (111) surface facets of six transition metals without considering vibrational contributions to the partition functions. See Table 1 for corresponding data that include vibrational contributions. The number of intermediate states between the reactant and transition states for eSMS calculations is determined by our desire to have an energy difference between intermediate states smaller than twice the thermal energy ($<2k_BT$). The aqueous-phase profiles portray the average of three or more independent eSMS calculations possessing 95% confidence intervals smaller than ±0.05 eV (see Table 1). The analogous plot for C–H bond cleavage reaction is provided in the Supplementary Fig. 1.

effects across metal surfaces. Given the absence of a linear $\Delta\Delta G^{act}$ dependence on H-bond or $\Delta G^{act,gas}$, we also studied all pairwise combinations of descriptors. Finally, we note here that we also analyzed the water orientation (H-up, H-down, parallel – see Supplementary Fig. 3) within the first water layer of the different surfaces in the reactant state (see height distribution function of water O in Supplementary Fig. 4); however, we did not observe any significant variation in water orientations across metals, explaining why we did not further study water orientation as a descriptor (Supplementary Table 10). Also, we attempted to use

Table 2 Average aqueous-phase effects on the activation free energy ($\Delta\Delta G^{act} = \Delta G^{act,liq} - \Delta G^{act,gas}$) as well as three solvation effect descriptors for the O–H and C–H bond cleavages of ethylene glycol over the (111) surface facet of six transition metals at 423 K (see Table 1 for 95% confidence intervals).

Cleavage	Surface	$\Delta\Delta G^{act}$, eV	$\Delta G^{act,gas}$, eV	H-bond	MC, e	BC, e
O–H	Ni	−0.21	0.70	0.99	0.64	−0.61
	Pd	−0.24	0.76	0.34	0.13	−0.36
	Pt	−0.45	0.68	0.54	−0.10	−0.24
	Cu	−0.55	1.08	0.77	0.69	−0.74
	Ag	−0.41	1.63	0.92	0.78	−0.77
	Au	−0.12	1.67	0.95	0.62	−0.63
C–H	Ni	−0.34	0.79	0.26	0.41	−0.36
	Pd	−0.02	0.83	−0.26	−0.03	0.06
	Pt	−0.15	0.71	0.12	0.08	0.03
	Cu	−0.37	1.43	0.21	0.53	−0.46
	Ag	−0.34	1.91	−0.27	0.28	−0.32
	Au	−0.26	1.69	−0.38	0.06	−0.12

$\Delta G^{act,gas}$ is the free energy of activation in vapor phase, H-bond denotes the change in mean of total hydrogen bonding (acceptor + donor) going from RS to TS, MC (molecular charge transfer) represents the change in the absolute sum of partial charges on the reacting moiety going from RS to TS, and finally BC (cleaving-bond charge transfer) is the change in sum of partial charges on the cleaving bond atoms (see Supplementary Table 5 for partial charges) going from RS to TS.

Fig. 3 Parity plot of the aqueous-phase effect on the activation free energy. The plot compares the aqueous-phase effect on activation free energy ($\Delta\Delta G^{act} = \Delta G^{act,liq} - \Delta G^{act,gas}$) computed by eSMS (QM/MM-FEP in Table 1) against the model-predicted aqueous-phase effect. The predicted values are calculated using the gas-phase free energy of activation ($\Delta G^{act,gas}$) and cleaving-bond charge transfer (BC) as two descriptors in (**a**) a linear model (eq. 1) for C–H bond cleavage and (**b**) a quadratic model (eq. 2) for O–H bond cleavage of ethylene glycol over the (111) surface facets of six transition metals at 423 K. The average aqueous-phase effect, $\overline{\Delta\Delta G^{act}}$, computed by eSMS, is −0.33 eV for O–H bond cleavage and −0.25 eV for C–H bond cleavage. The mean of absolute errors (MAE) between eSMS and model-predicted values is 0.03 eV in the linear model (**a**) and 0.02 eV in the quadratic model (**b**). The corresponding model parameters are listed in Supplementary Tables 7 and 8.
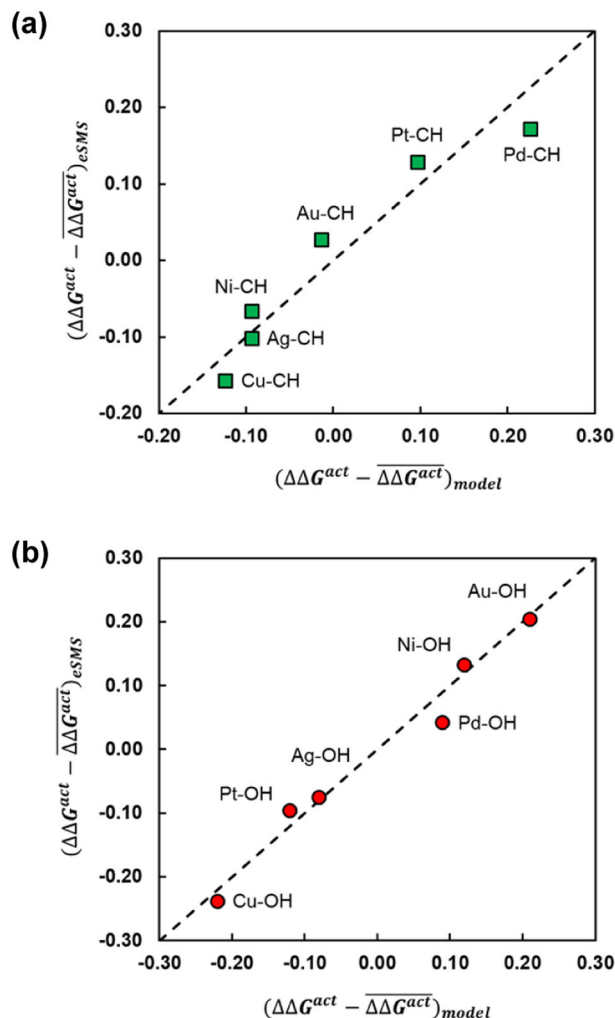
the standard electrode potential of the metal elements as descriptor but again no meaningful correlation could be obtained such that it is not further discussed.

Next, we first examined the pairwise correlations between the descriptors using the Pearson correlation coefficient (PCC)[68]. The results (see Supplementary Table 6) indicate that BC and MC are totally correlated (PCC ~ −1.0), which is expected given that they both describe charge transfer. In addition, H-bond is more correlated with MC and BC in the O–H bond cleavage than in the C–H bond cleavage. We attribute this to the fact that hydrogen bonding is obtained from the interaction of water molecules with the OH functional groups of EG, and the O–H bond cleavage reaction causes a significant change in the charges on one of the two O–H functional groups in EG in the TS. Finally, $\Delta G^{act,gas}$ is hardly correlated with BC, MC or H-bond in both cleavages.

Second, using a simple linear model (Eq. 1), we investigated the relation between the descriptors and the aqueous-phase effects on the free energies of activation ($\Delta\Delta G^{act}$). We emphasize that we do not intend to quantitatively predict $\Delta\Delta G^{act}$ using a set of descriptors. Instead, we employ models based on physics-based descriptors to explain what physical phenomena could explain the changes in solvation effects on the kinetics of the studied surface-catalyzed reactions.

$$\left(\Delta\Delta G^{act} - \overline{\Delta\Delta G^{act}}\right)_{model} = \alpha_1(f_1 - \overline{f_1}) + \alpha_2(f_2 - \overline{f_2}) \quad (1)$$

In eq. 1, bar signs show the mean of the corresponding variable, α_1 and α_2 are model parameters, and f_1 and f_2 represent descriptors (Table 2). The best-fitting parameters and mean absolute error (MAE) of the linear model for different combinations of descriptors are listed in Supplementary Table 7. Interestingly, the linear model can estimate $\Delta\Delta G^{act}$ very well for the C–H bond cleavage but not for the O–H bond cleavage. As expected, the dominant factor in C–H bond cleavage is the charge-transfer effect; that is, $\alpha_2 \gg \alpha_1$ when one of charge-transfer effect descriptors (BC or MC) used as f_2 (see Supplementary Table 7). Finally, a quadratic model with two

descriptors was employed to explain $\Delta\Delta G^{act}$ of the O–H bond cleavage.

$$\left(\Delta\Delta G^{act} - \overline{\Delta\Delta G^{act}}\right)_{model} = \alpha_1(f_1 - \overline{f_1}) + \alpha_2(f_2 - \overline{f_2}) + \alpha_3(f_1 - \overline{f_1})^2 + \alpha_4(f_2 - \overline{f_2})^2 \quad (2)$$

The results of this model for different combinations of descriptors are included in Supplementary Table 8.

Overall, when comparing the model parameters of the linear and quadratic fits, we conclude that the aqueous-phase effect on the free energy of activation of O–H and C–H bond cleavages of EG over the investigated metal surfaces originates primarily from some form of a charge-transfer effect (BC or MC) (more charge transfer in the TS relative to the RS leads to more stabilization)

and partly on another descriptor that could be related to H-bond and $\Delta G^{act,gas}$ (larger barriers are more stabilized). Figure 3 presents the computed aqueous-phase effect by eSMS versus the estimated one from a linear fit for C–H bond cleavage and a quadratic fit for O–H bond cleavage, in which BC and $\Delta G^{act,gas}$ were used as descriptors.

Comparison to implicit solvation models. Finally, the implicit solvation models (iSMS[69] and VASPsol[70,71]) failed to capture the full solvent stabilization during the O–H bond cleavage of EG (see Table 1). For the C–H bond cleavage, implicit and explicit solvation models anticipate comparable aqueous-phase effects for the metals that display a smaller charge transfer effect (Pd, Pt, Au). Supplementary Table 9 illustrates that this observation holds even when considering typical uncertainties in cavity radius of ±10% for transition metal elements. In short, the reliability of implicit solvation calculations for heterogeneous (metal) catalysis applications is currently limited (unknown) due to the very limited availability of experimental data that can be used in the parameterization of the implicit solvation models. This appears to be currently an advantage for explicit solvation models that rely "only" on a meaningful potential energy description.

Discussion

In summary, we hypothesized that since solvents can modify the electronic structure of a metal surface, thereby affecting the stability of reacting moieties, the metal identity plays a significant role for solvation effects on elementary reactions. We investigated aqueous-phase effects on the free energy of activation of the initial O–H and C–H bond cleavages of ethylene glycol over the (111) surface of six transition metals, including Ni, Pd, Pt, Cu, Ag, and Au, to disclose the role of metal identity on solvation effects. To compute the free energy of activation in the presence of water, we utilized our explicit solvation approach, named eSMS, which is based on a hybrid quantum mechanical/molecular mechanical (QM/MM) description of the potential energy surface. Our hypothesis was confirmed by finding significantly different aqueous-phase effects on the activation barrier ($\Delta\Delta G^{act} = \Delta G^{act,}$ $_{liq} - \Delta G^{act,gas}$) for the same bond cleavage across different metals, suggesting that solvation effects have to be studied in detail for any specific reaction system. Subsequently, by introducing three intuitive, physics-based descriptors, the charge-transfer effect, hydrogen bonding, and the gas-phase activation free energy barrier, and studying correlations between the aqueous-phase effects and these descriptors, we can conclude that the aqueous-phase effects originate primarily from various charge-transfer effects across the different metals, and to a lesser extent to another descriptor that could be related to a different amount of hydrogen bonding and the gas-phase activation barriers across the different metals. This observation agrees with previous AIMD simulations of oxygen activation over Au catalysts[17]. Finally, implicit solvation models are currently not able to capture these charge-transfer effects that can lead to changes in preference of initial O–H versus C–H bond cleavage in alcohols over various transition metal surfaces.

Methods

Planewave DFT calculations. Vapor-phase DFT calculations were carried out using periodic boundary conditions as implemented in the Vienna Ab Initio Simulation Package (VASP 5.4.4)[72,73]. A frozen-core, all-electron projector augmented-wave (PAW)[74] method was utilized to avoid the singularities of Kohn–Sham wavefunctions at the nuclear positions. The number of valence electrons considered for Ni, Pd, Pt, Cu, Ag, Au, C, O, and H are 10, 10, 10, 11, 11, 11, 4, 6, and 1, respectively. The unknown part of interaction energy between individual electrons, i.e., the exchange-correlation functional, was expressed using the Perdew–Burke–Ernzerhof (PBE)[75,76] functional within the semi-local generalized gradient approximation[77]. Brillouin zone integrations have been performed with a

$4 \times 4 \times 1$ Monkhorst–Pack[78] k-point grid and electronic wavefunctions at each k-point were expanded using a discrete plane-wave basis set with kinetic energies limited to 400 eV. A first order smearing method (Methfessel–Paxton)[79] with 0.10 eV smearing width was employed, allowing to accurately calculate the entropic contributions due to the smearing. Dipole and quadrupole corrections (along the surface normal) to the total energy have been calculated using a modified version of the Makov–Payne[80] method, and Harris corrections, based on the non-self-consistent Harris–Foulkes[81,82] functional, have been applied to the stress-tensor and forces. A 4×4-unit cell with four layers of metal atoms (bottom two layers fixed in their bulk positions) has been employed. By introducing a 15 Å vacuum on top of the surface, the interaction between the periodic images along the surface normal has been curtailed. A self-consistent field (SCF) convergence criterion for the electronic degrees of freedom of the valence electrons was set to 1.0×10^{-7} eV. Transition state structures for the elementary processes were located using a combination of climbing-image nudged elastic band[83,84] and dimer[85,86] methods. Finally, the minima and the first order saddle points were validated by computing the Hessian matrix and vibrational spectra. We note that spin-polarized calculations have been carried out for the Ni surface.

Non-periodic cluster calculations. Cluster model DFT calculations in vacuum have been carried out using the TURBOMOLE 7.2 program package[87–89]. To model the cluster surfaces, two layers of metal atoms with a hexagonal shaped geometry (51 atoms) were chosen. The convergence of the total QM/MM energy with respect to the lateral size and depth of the cluster geometry can be found elsewhere[54]. An improved version of the default TURBOMOLE basis sets (def-bases) with split valence and polarization functions (def2-SVP)[90,91] were employed to represent the adsorbate atoms and the metal atoms of Ni and Cu. Furthermore, Ag, Pd, Pt, and Au atoms were represented using scalar relativistic effective core potentials (ECPs) in conjunction with split valence basis sets augmented by polarization functions[91,92]. Electron exchange and correlation effects were accounted for by employing the PBE functional[75,76]. To speed up the calculation as recommended by TURBOMOLE, the RI-J approximation with auxiliary basis sets was used to approximate the coulomb integrals[93,94]. An SCF convergence criterion of 1.0×10^{-7} Hartree was established and a Gauss-Chebyshev type spherical grid, m4, was employed to perform the numerical integrations[88].

Molecular dynamics (MD) simulations. MD simulations were carried out using the DL_POLY 4.03 molecular simulation program package[95]. The initial 4×4 unit cell for each metal surface was augmented laterally to a 16×20 surface with further vacuum added in the Z-direction resulting in a simulation box comprising of 1280 metal atoms. The simulation box size for each metal is reported in Supplementary Table 1. The simulation box height was selected based on the work from Behler et al.[67] finding that simulations of metal-water interfaces should contain a water layer of ~40 Å height. The experimental saturated liquid water density of ~0.9 g/cm^3 at 423 K was achieved by packing the simulation box of Ni, Pd, Pt, Cu, Ag, and Au with 2258, 2758, 2800, 2398, 3045, and 2985 water molecules, respectively. All metal and adsorbate atoms were kept fixed while the geometry of water molecules was constricted to that of TIP3P[96] geometry with the RATTLE algorithm[97]. To solve the Newton's equations of motion, a velocity version of the SHAKE algorithm[98], in conjunction with the velocity Verlet (VV) integrator[99] were used. The TIP3P model was employed for the force field parameters of liquid water while the van der Waals parameters for adsorbate atoms were obtained from the OPLS force field[100,101]. In addition to the OPLS parameters, the Lennard-Jones parameters from the Combined B3LYP/6-31_G*/AMBER Potential[102] were used for the hydrogen atoms of the adsorbed moieties. Lennard-Jones parameters for hydrogen atoms are important in QM/MM optimizations that permit hydrogen atoms to approach water molecules and leave the protective environment of a neighboring carbon or oxygen atom. The Lennard-Jones metal potential[103] was employed to describe the metal-water interaction. The LJ cross-term of intermolecular parameters were calculated by Lorentz-Berthelot mixing rules through equations $\sigma_{ij} = \frac{\sigma_i + \sigma_j}{2}$ and $\varepsilon_{ij} = \sqrt{\varepsilon_i \varepsilon_j}$. All Lennard-Jones parameters are included in Supplementary Table 2. The charges for the QM atoms were estimated using the natural population analysis (NPA)[66]. To describe the interaction of the TIP3P water point charges with the quantum chemically described cluster model, we employed the periodic electrostatic embedded cluster method (PEECM)[104] as implemented in TURBOMOLE. Simulations were carried out in a canonical ensemble (NVT) with Nosé-Hoover thermostat[105,106]. A 1 ps relaxation time constant for temperature fluctuations was used to maintain the average system temperature. Electrostatic interactions were accounted for by using the Smoothed Particle Mesh Ewald (SPME) method[107] with automatic parameter optimization for default SPME precision and a 12 Å cutoff radius was adopted for the van der Waals interactions and the transition between short and long-range electrostatic interactions. Unless specified otherwise, for each free energy perturbation step, all systems were equilibrated for 250 ps and sampled for 1000 ps (1ns) using a 1 fs timestep to obtain 1000 MM conformations (1 ps apart). Thus, MD simulations for over 2.9 ms were performed for this study. To optimize structures in an aqueous reaction environment, we utilized the fixed-size ensemble approximation with 5000 MM conformations (250 ps equilibration and 5 ns sampling) recorded every 1 ps.

QM/MM energy calculation. The QM/MM minimum free energy path (QM/MM-MFEP)[52,53] method for optimizing the intrinsic reaction coordinate on a potential of mean force (PMF) description of the reaction system has been implemented in our program packages. A full description of this methodology, eSMS (Explicit Solvation for Metal Surfaces) can be found elsewhere[54]. Briefly, the total energy function formulation of our eSMS method is given by

$$
\begin{aligned}
E_T\left(\underline{r}_{QM}, \underline{r}_{MM}\right) = {}& E_{QM}^{Surface}\left(\underline{r}_{QM}\right) - E_{QM}^{cluster}\left(\underline{r}_{QM}\right) + \langle\Psi|H_{eff}\left(\underline{r}_{QM}, \underline{r}_{MM}^{MeanField(100)}\right)|\Psi\rangle \\
& + \left[\frac{1}{100}\sum_{j=1}^{100}\left[E_{j,MM+QM/MM}^{elec+vdW}\left(\underline{r}_{QM}, \underline{r}_{MM}^{MeanField(100)}\right)\right]\right]_{Q_i=0, i\in QM} \\
& - E_{j,MM+QM/MM}^{elec+vdW}\left(\underline{r}_{QM}, \underline{r}_{MM}^{MeanField(100)}\right) + E_{j,MM+QM/MM}^{elec+vdW}\left(\underline{r}_{QM}, \underline{r}_{MM}\right)
\end{aligned}
\tag{3}
$$

where the first term is evaluated for a periodic slab using the VASP program package (*planewave DFT calculation*), the second term is a QM calculation in vacuum computed with the TURBOMOLE program package (*non-periodic cluster calculations*), and the third term is a QM cluster calculation in a periodic mean field of MM water molecules computed using the periodic electrostatic embedded cluster method (PEECM) in TURBOMOLE under the fixed-charge approximation (fixed-charge approximation has been validated for our eSMS approach[54]). We note that the number 100 in the equation indicates that 100 MM conformations, selected equally spaced from equilibrated 1 ns molecular dynamic (MD) simulations (10 ps apart), were used to represent the mean field of the MM water molecules. Finally, the last three terms account for the classical (MM level of theory) electrostatic and van-der-Waals interaction energy of the total system without overcounting the electrostatic interaction of the MM (water) molecules with the QM cluster subsystem. We note that all solvent (water) molecules are described in this study at the MM level of theory.

Free energy calculations require energy evaluation from uncorrelated measurements of the system and ideally the energy estimator should also be capable of minimizing the statistical bias and variance of the free energy differences of the physical system being studied. Exponential averaging (EXP), also known as the Zwanzig relationship[108] has long been applied to study a variety of problems such as amino acid recognition[109], RAS-RAF binding affinity[110], and octanol/water partition coefficients[111], etc. However, the EXP has been shown to represent poor efficiency and phase space overlap[112,113], and is also largely dependent on the distribution of the QM/MM energy[114]. Here, we employed the Bennett Acceptance Ratio (BAR)[115] as the free energy estimator which uses both the forward and reverse distributions simultaneously in a more efficient way than simply averaging the forward and reverse exponential estimators. BAR has been demonstrated to benefit from a lower bias and variance of the free energy estimates in practical atomistic simulations when compared to EXP and thermodynamic integration (TI)[112,116]. Finally, the whole free energy estimation procedure has been repeated three times independently to establish 95% confidence intervals for evaluating the free energy of activation, assuming a normal distribution[117]. More independent simulations were carried out only if these three experiments were not resulting in 95% confidence interval smaller than 0.05 eV. All uncertainties reported in this study are 95% confidence intervals.

Average rotational correlation time. Adequately sampling of the potential energy surface for all relevant configurations of the system is of great importance in any QM/MM approach for computing the liquid-phase effect on the free energy of elementary processes[114]. Owing to a lack of consensus on how much sampling of the configurational space is sufficient for a solvated adsorbed carbohydrate species on a metal surface for an error smaller than 0.05 eV, we computed the average rotational correlation time for water molecules in close proximity (up to 5 Å) to adsorbed ethylene glycol in the reactant and transition states over the (111) facet of six transition metals and reported them in Supplementary Table 3. The longest average correlation time is computed to be ~200 ps. Hence, we decided to sample for 1000 ps to make sure that relevant configurations of the systems are sampled adequately. As discussed above, for free-energy calculations, the procedure was repeated at least three times with independent MD trajectories to establish the confidence interval of the computation of the free energy of activation in aqueous phase.

Non-periodic implicit solvation calculations. The implicit solvation model for solid surfaces (iSMS)[69] was utilized to compute the activation free energies in an aqueous reaction environment as

$$
\Delta G_{solvent}^{\ddagger} = \Delta G_{Gas}^{\ddagger} + \left[G_{solvent}^{TS} - G_{solvent}^{IS}\right]
\tag{4}
$$

where $\Delta G_{Gas}^{\ddagger}$ is the respective activation free energy under gas phase conditions, and $G_{solvent}^{IS}$ and $G_{solvent}^{TS}$ represent the solvation free energies of initial and transition states, respectively, computed as

$$
G_{surface+intermediate}^{liquid} = G_{surface+intermediate}^{vacuum} + \left(G_{cluster+intermediate}^{liquid} - E_{cluster+intermediate}^{vacuum}\right)
\tag{5}
$$

where $G_{surface+intermediate}^{vacuum}$ is the free energy of an intermediate (e.g., IS or TS) in the absence of a solvent, computed here within the harmonic approximation using

plane-wave DFT calculations for periodic slab models, $G_{cluster+intermediate}^{liquid}$ is the free energy of the metal cluster and surface intermediate in liquid without vibrational contributions (that are already considered in the first term), and $E_{cluster+intermediate}^{vacuum}$ is the DFT energy of the same cluster in the absence of the solvent. To compute the $G_{cluster+intermediate}^{liquid}$ term, COSMO-RS[118,119] (conductor-like screening model for real solvents) calculations are performed using the COSMOtherm program with latest FINE parameterization[120]. The COSMOtherm program for solvent thermodynamic properties requires COSMO calculations to be performed at the BP-TZVPD level of theory. Given the uncertainty in cavity radius for transition metal elements, calculations are performed with default and 10% increased and decreased cavity radius for the transition metal elements (see Supplementary Table 9).

Periodic Implicit Solvation Calculations. In addition to implicit solvation calculations performed with iSMS method, implicit solvation calculations were also performed with VASPsol[70,71] using a relative permittivity of water of 44.07 at 423 K[121]. For VASPsol, we used the default values for the parameter n_c that defines the value at which the dielectric cavity forms and for the width of the diffuse cavity, σ, and for effective surface tension parameter, τ, describing the cavitation, dispersion, and repulsive interaction between the solute and the solvent that are not captured by the electrostatic terms[71]. While the parameters are likely most accurate only for simulations at 298 K and not at 423 K, they are the optimized parameters of the solvent model that cannot easily be obtained at other temperatures. Due to the absence of adequate experimental solvation data at 423 K, we decided that the default parameters are likely most meaningful, i.e., the relative permittivity is the only temperature dependent solvent parameter in our VASPsol model. All other computational details for periodic implicit solvation calculations were kept the same as in our periodic vapor-phase calculations.

Data availability
The authors declare that the data supporting the findings of this study are available within the paper and its supplementary information files. We note that the optimized atomic coordinates of reactant (RS) and transition states (TS) clusters in gas and liquid phase are provided in Supplementary Data 1 file.

References
1. Verdasco, G., Martin, M. A., Delcastillo, B., Lopezalvarado, P. & Menendez, J. C. Solvent effects on the fluorescent emission of some new benzimidazole derivatives. *Analytica Chim. Acta* **303**, 73–78 (1995).
2. Fung, H. L. & Nealon, T. Solvent effects on comparative dissolution of pharmaceutical solvates. *Chem. Pharm. Bull.* **22**, 454–458 (1974).
3. Jenke, D., Odufu, A. & Poss, M. The effect of solvent polarity on the accumulation of leachables from pharmaceutical product containers. *Eur. J. Pharm. Sci.* **27**, 133–142 (2006).
4. Patil S., Patil S. & Navale S. Effect of Solvent and Crystallization Method on Physicochemical Properties of Aceclofenac and Fenofibrate. *Br. J. Pharm. Res.* **12**, 1–8 (2016).
5. Beilin, E., Baker, L. J., Aikins, J. & Baryla, N. E. Effect of incomplete removal of the tert-butoxycarbonyl protecting group during synthesis of a pharmaceutical drug substance on the residual solvent analysis. *J. Pharm. Biomed. Anal.* **52**, 316–319 (2010).
6. Mota, F. L., Carneiro, A. R., Queimada, A. J., Pinho, S. P. & Macedo, E. A. Temperature and solvent effects in the solubility of some pharmaceutical compounds: Measurements and modeling. *Eur. J. Pharm. Sci.* **37**, 499–507 (2009).
7. Chen, L. D., Urushihara, M., Chan, K. R. & Norskov, J. K. Electric Field Effects in Electrochemical CO2 Reduction. *ACS Catal.* **6**, 7133–7139 (2016).
8. Cheng, T., Xiao, H. & Goddard, W. A. Free-Energy Barriers and Reaction Mechanisms for the Electrochemical Reduction of CO on the Cu(100) Surface, Including Multiple Layers of Explicit Solvent at pH 0. *J. Phys. Chem. Lett.* **6**, 4767–4773 (2015).
9. Goldsmith, Z. K., Secor, M. & Hammes-Schiffer, S. Inhomogeneity of Interfacial Electric Fields at Vibrational Probes on Electrode Surfaces. *ACS Cent. Sci.* **6**, 304–311 (2020).
10. Otani, M. et al. Structure of the water/platinum interface - a first principles simulation under bias potential. *Phys. Chem. Chem. Phys.* **10**, 3609–3612 (2008).
11. Zope, B. N., Hibbitts, D. D., Neurock, M. & Davis, R. J. Reactivity of the Gold/Water Interface During Selective Oxidation Catalysis. *Science* **330**, 74–78 (2010).
12. Yoon, Y., Rousseau, R., Weber, R. S., Mei, D. H. & Lercher, J. A. First-Principles Study of Phenol Hydrogenation on Pt and Ni Catalysts in Aqueous Phase. *J. Am. Chem. Soc.* **136**, 10287–10298 (2014).

13. Tupy, S. A. et al. Correlating Ethylene Glycol Reforming Activity with In Situ EXAFS Detection of Ni Segregation in Supported NiPt Bimetallic Catalysts. *ACS Catal.* **2**, 2290–2296 (2012).

14. Saleheen, M. & Heyden, A. Liquid-Phase Modeling in Heterogeneous Catalysis. *ACS Catal.* **8**, 2188–2194 (2018).

15. Karim, A. M. et al. In Situ X-ray Absorption Fine Structure Studies on the Effect of pH on Pt Electronic Density during Aqueous Phase Reforming of Glycerol. *ACS Catal.* **2**, 2387–2394 (2012).

16. Miller, K. L., Lee, C. W., Falconer, J. L. & Medlin, J. W. Effect of water on formic acid photocatalytic decomposition on TiO_2 and Pt/TiO_2. *J. Catal.* **275**, 294–299 (2010).

17. Siemer, N., Muñoz-Santiburcio, D. & Marx, D. Solvation-Enhanced Oxygen Activation at Gold/Titania Nanocatalysts. *ACS Catal.* **10**, 8530–8534 (2020).

18. Singh, N. et al. Quantifying Adsorption of Organic Molecules on Platinum in Aqueous Phase by Hydrogen Site Blocking and in Situ X-ray Absorption Spectroscopy. *ACS Catal.* **9**, 6869–6881 (2019).

19. Akinola, J., Barth, I., Goldsmith, B. R. & Singh, N. Adsorption Energies of Oxygenated Aromatics and Organics on Rhodium and Platinum in Aqueous Phase. *ACS Catal.* **10**, 4929–4941 (2020).

20. Behtash, S. et al. Solvation Effects in the Hydrodeoxygenation of Propanoic Acid over a Model Pd(211) Catalyst. *J. Phys. Chem. C* **120**, 2724–2736 (2016).

21. Rajadhyaksha, R. A. & Karwa, S. L. Solvent Effects in Catalytic-Hydrogenation. *Chem. Eng. Sci.* **41**, 1765–1770 (1986).

22. Mukherjee, S. & Vannice, M. A. Solvent effects in liquid-phase reactions - I. Activity and selectivity during citral hydrogenation on Pt/SiO_2 and evaluation of mass transfer effects. *J. Catal.* **243**, 108–130 (2006).

23. Akpa, B. S. et al. Solvent effects in the hydrogenation of 2-butanone. *J. Catal.* **289**, 30–41 (2012).

24. McManus, I. et al. Effect of solvent on the hydrogenation of 4-phenyl-2-butanone over Pt based catalysts. *J. Catal.* **330**, 344–353 (2015).

25. Knowles, W. S. Asymmetric hydrogenation. *Acc. Chem. Res.* **16**, 106–112 (1983).

26. Valgimigli, L., Banks, J. T., Ingold, K. U. & Lusztyk, J. Kinetic Solvent Effects on Hydroxylic Hydrogen-Atom Abstractions Are Independent of the Nature of the Abstracting Radical - 2 Extreme Tests Using Vitamin-E and Phenol. *J. Am. Chem. Soc.* **117**, 9966–9971 (1995).

27. Wiebus, E. & Cornils, B. Industrial-Scale Oxo Synthesis with an Immobilized Catalyst. *Chem.-Ing.-Tech.* **66**, 916–923 (1994).

28. Beller, M., Cornils, B., Frohning, C. D. & Kohlpaintner, C. W. Progress in Hydroformylation and Carbonylation. *J. Mol. Catal. a-Chem.* **104**, 17–85 (1995).

29. Dyson, P. J. & Jessop, P. G. Solvent effects in catalysis: rational improvements of catalysts via manipulation of solvent interactions. *Catal. Sci. Technol.* **6**, 3302–3316 (2016).

30. Cornils, B., Herrmann, W. A. & Eckl, R. W. Industrial aspects of aqueous catalysis. *J. Mol. Catal. A* **116**, 27–33 (1997).

31. Zhang, L. et al. Correlation of Pt-Re surface properties with reaction pathways for the aqueous-phase reforming of glycerol. *J. Catal.* **287**, 37–43 (2012).

32. He, R., Davda, R. R. & Dumesic, J. A. In situ ATR-IR spectroscopic and reaction kinetics studies of water-gas shift and methanol reforming on Pt/Al_2O_3 catalysts in vapor and liquid phases. *J. Phys. Chem. B* **109**, 2810–2820 (2005).

33. Taylor, C. D. & Neurock, M. Theoretical insights into the structure and reactivity of the aqueous/metal interface. *Curr. Opin. Solid State Mater. Sci.* **9**, 49–65 (2005).

34. Faheem, M., Saleheen, M., Lu, J. M. & Heyden, A. Ethylene glycol reforming on Pt(111): first-principles microkinetic modeling in vapor and aqueous phases. *Catal. Sci. Technol.* **6**, 8242–8256 (2016).

35. Bertero, N. M., Trasarti, A. F., Acevedo, M. C., Marchi, A. J. & Apesteguia, C. R. Solvent effects in solid acid-catalyzed reactions: The case of the liquid-phase isomerization/cyclization of citronellal over SiO_2-Al_2O_3. *Mol. Catal.* **481**, 110192 (2020).

36. Faveere, W. et al. Glycolaldehyde as a Bio-Based C-2 Platform Chemical: Catalytic Reductive Amination of Vicinal Hydroxyl Aldehydes. *ACS Catal.* **10**, 391–404 (2020).

37. Saleheen, M., Verma, A. M., Mamun, O., Lu, J. & Heyden, A. Investigation of solvent effects on the hydrodeoxygenation of guaiacol over Ru catalysts. *Catal. Sci. Technol.* **9**, 6253–6273 (2019).

38. Zhao, J. J. et al. Suppressing Metal Leaching in a Supported Co/SiO_2 Catalyst with Effective Protectants in the Hydroformylation Reaction. *ACS Catal.* **10**, 914–920 (2020).

39. Kulal, A. B., Kasabe, M. M., Jadhav, P. V., Dongare, M. K. & Umbarkar, S. B. Hydrophobic WO_3/SiO_2 catalyst for the nitration of aromatics in liquid phase. *Appl. Catal. A* **574**, 105–113 (2019).

40. Staszak-Jirkovsky, J. et al. Water as a Promoter and Catalyst for Dioxygen Electrochemistry in Aqueous and Organic Media. *ACS Catal.* **5**, 6600–6607 (2015).

41. Wan, H., Vitter, A., Chaudhari, R. V. & Subramaniam, B. Kinetic investigations of unusual solvent effects during Ru/C catalyzed hydrogenation of model oxygenates. *J. Catal.* **309**, 174–184 (2014).

42. Mellmer, M. A. et al. Solvent Effects in Acid-Catalyzed Biomass Conversion Reactions. *Angew. Chem. Int. Ed.* **53**, 11872–11875 (2014).

43. Zare, M., Solomon, R. V., Yang, W., Yonge, A. & Heyden, A. Theoretical Investigation of Solvent Effects on the Hydrodeoxygenation of Propionic Acid over a Ni(111) Catalyst Model. *J. Phys. Chem. C* **124**, 16488–16500 (2020).

44. Car, R. & Parrinello, M. Unified Approach for Molecular-Dynamics and Density-Functional Theory. *Phys. Rev. Lett.* **55**, 2471–2474 (1985).

45. Carloni, P., Rothlisberger, U. & Parrinello, M. The Role and Perspective of Ab Initio Molecular Dynamics in the Study of Biological Systems. *Acc. Chem. Res.* **35**, 455–464 (2002).

46. Iftimie, R., Minary, P. & Tuckerman, M. E. Ab initio molecular dynamics: Concepts, recent developments, and future trends. *Proc. Natl Acad. Sci. USA* **102**, 6654–6659 (2005).

47. Mattsson, T. R. & Paddison, S. J. Methanol at the water-platinum interface studied by ab initio molecular dynamics. *Surf. Sci.* **544**, L697–L702 (2003).

48. Yang, J., Dauenhauer, P. J. & Ramasubramaniam, A. The role of water in the adsorption of oxygenated aromatics on Pt and Pd. *J. Comput. Chem.* **34**, 60–66 (2013).

49. Klamt, A. Conductor-Like Screening Model for Real Solvents - a New Approach to the Quantitative Calculation of Solvation Phenomena. *J. Phys. Chem.* **99**, 2224–2235 (1995).

50. Klamt, A. & Schuurmann, G. Cosmo - a New Approach to Dielectric Screening in Solvents with Explicit Expressions for the Screening Energy and Its Gradient. *J. Chem. Soc. Perkin Trans.* **2**, 799–805 (1993).

51. Zhang, Y. K., Liu, H. Y. & Yang, W. T. Free energy calculation on enzyme reactions with an efficient iterative procedure to determine minimum energy paths on a combined ab initio QM/MM potential energy surface. *J. Chem. Phys.* **112**, 3483–3492 (2000).

52. Hu, H., Lu, Z. Y., Parks, J. M., Burger, S. K. & Yang, W. T. Quantum mechanics/molecular mechanics minimum free-energy path for accurate reaction energetics in solution and enzymes: Sequential sampling and optimization on the potential of mean force surface. *J. Chem. Phys.* **128**, 034105:034101–034105:034118 (2008).

53. Hu, H., Lu, Z. Y. & Yang, W. T. QM/MM minimum free-energy path: Methodology and application to triosephosphate isomerase. *J. Chem. Theory Comput* **3**, 390–406 (2007).

54. Faheem, M. & Heyden, A. Hybrid Quantum Mechanics/Molecular Mechanics Solvation Scheme for Computing Free Energies of Reactions at Metal-Water Interfaces. *J. Chem. Theory Comput.* **10**, 3354–3368 (2014).

55. Saleheen, M., Zare, M., Faheem, M. & Heyden, A. Computational Investigation of Aqueous Phase Effects on the Dehydrogenation and Dehydroxylation of Polyols over Pt(111). *J. Phys. Chem. C* **123**, 19052–19065 (2019).

56. Breslow, R. & Guo, T. Diels-Alder Reactions in Nonaqueous Polar-Solvents - Kinetic Effects of Chaotropic and Antichaotropic Agents and of Beta-Cyclodextrin. *J. Am. Chem. Soc.* **110**, 5613–5617 (1988).

57. Li, Y. et al. Solvent effects on heterogeneous catalysis in the selective hydrogenation of cinnamaldehyde over a conventional Pd/C catalyst. *Catal. Sci. Technol.* **8**, 3580–3589 (2018).

58. Ebbesen, S. D., Mojet, B. L. & Lefferts, L. In situ ATR-IR study of CO adsorption and oxidation over Pt/Al2O3 in gas and aqueous phase: Promotion effects by water and pH. *J. Catal.* **246**, 66–73 (2007).

59. Deshpande, S. & Greeley, J. First-Principles Analysis of Coverage, Ensemble, and Solvation Effects on Selectivity Trends in NO Electroreduction on Pt3Sn Alloys. *ACS Catal.* **10**, 9320–9327 (2020).

60. Clayborne, A., Chun, H.-J., Rankin, R. B. & Greeley, J. Elucidation of Pathways for NO Electroreduction on Pt(111) from First Principles. *Angew. Chem. Int. Ed.* **54**, 8255–8258 (2015).

61. Kim, S. et al. Recent advances in hydrodeoxygenation of biomass-derived oxygenates over heterogeneous catalysts. *Green. Chem.* **21**, 3715–3743 (2019).

62. Salciccioli, M. & Vlachos, D. G. Kinetic Modeling of Pt Catalyzed and Computation-Driven Catalyst Discovery for Ethylene Glycol Decomposition. *ACS Catal.* **1**, 1246–1256 (2011).

63. Salciccioli, M. & Vlachos, D. G. Correction to Kinetic Modeling of Pt Catalyzed and Computation-Driven Catalyst Discovery for Ethylene Glycol Decomposition. *ACS Catal.* **2**, 306–306 (2012).

64. Salciccioli, M., Yu, W., Barteau, M. A., Chen, J. G. & Vlachos, D. G. Differentiation of O–H and C–H Bond Scission Mechanisms of Ethylene Glycol on Pt and Ni/Pt Using Theory and Isotopic Labeling Experiments. *J. Am. Chem. Soc.* **133**, 7996–8004 (2011).

65. Zhang, X., DeFever, R. S., Sarupria, S. & Getman, R. B. Free Energies of Catalytic Species Adsorbed to Pt(111) Surfaces under Liquid Solvent Calculated Using Classical and Quantum Approaches. *J. Chem. Inf. Modeling* **59**, 2190–2198 (2019).

66. Reed, A. E., Weinstock, R. B. & Weinhold, F. Natural-Population Analysis. *J. Chem. Phys.* **83**, 735–746 (1985).

67. Natarajan, S. K. & Behler, J. Neural network molecular dynamics simulations of solid-liquid interfaces: water at low-index copper surfaces. *Phys. Chem. Chem. Phys.* **18**, 28704–28725 (2016).

68. Kirch, W. (ed) in *Encyclopedia of Public Health* (Springer, the Netherlands, 2008).

69. Faheem, M., Suthirakun, S. & Heyden, A. New Implicit Solvation Scheme for Solid Surfaces. *J. Phys. Chem. C* **116**, 22458–22462 (2012).

70. Fishman, M., Zhuang, H. L. L., Mathew, K., Dirschka, W., Hennig, R. G. Accuracy of exchange-correlation functionals and effect of solvation on the surface energy of copper. *Phys. Rev. B* **87**, 245402 (2013).

71. Mathew, K., Sundararaman, R., Letchworth-Weaver, K., Arias, T. A. & Hennig, R. G. Implicit solvation model for density-functional study of nanocrystal surfaces and reaction pathways. *J. Chem. Phys.* **140**, 084106:084101–084106:084108 (2014).

72. Kresse, G. & Furthmuller, J. Efficiency of ab-initio total energy calculations for metals and semiconductors using a plane-wave basis set. *Comp. Mater. Sci.* **6**, 15–50 (1996).

73. Kresse, G. & Furthmuller, J. Efficient iterative schemes for ab initio total-energy calculations using a plane-wave basis set. *Phys. Rev. B* **54**, 11169–11186 (1996).

74. Blochl, P. E. Projector Augmented-Wave Method. *Phys. Rev. B* **50**, 17953–17979 (1994).

75. Perdew, J. P. & Yue, W. Accurate and Simple Density Functional for the Electronic Exchange Energy - Generalized Gradient Approximation. *Phys. Rev. B* **33**, 8800–8802 (1986).

76. Perdew, J. P. & Wang, Y. Accurate and Simple Analytic Representation of the Electron-Gas Correlation-Energy. *Phys. Rev. B* **45**, 13244–13249 (1992).

77. Perdew, J. P., Burke, K. & Ernzerhof, M. Generalized gradient approximation made simple. *Phys. Rev. Lett.* **77**, 3865–3868 (1996).

78. Monkhorst, H. J. & Pack, J. D. Special Points for Brillouin-Zone Integrations. *Phys. Rev. B* **13**, 5188–5192 (1976).

79. Methfessel, M. & Paxton, A. T. High-Precision Sampling for Brillouin-Zone Integration in Metals. *Phys. Rev. B* **40**, 3616–3621 (1989).

80. Makov, G. & Payne, M. C. Periodic Boundary-Conditions in Ab-Initio Calculations. *Phys. Rev. B* **51**, 4014–4022 (1995).

81. Harris, J. Simplified Method for Calculating the Energy of Weakly Interacting Fragments. *Phys. Rev. B* **31**, 1770–1779 (1985).

82. Matthew, W., Foulkes, C. & Haydock, R. Tight-Binding Models and Density-Functional Theory. *Phys. Rev. B* **39**, 12520–12536 (1989).

83. Henkelman, G. & Jonsson, H. Improved tangent estimate in the nudged elastic band method for finding minimum energy paths and saddle points. *J. Chem. Phys.* **113**, 9978–9985 (2000).

84. Henkelman, G., Uberuaga, B. P. & Jonsson, H. A climbing image nudged elastic band method for finding saddle points and minimum energy paths. *J. Chem. Phys.* **113**, 9901–9904 (2000).

85. Henkelman, G. & Jonsson, H. A dimer method for finding saddle points on high dimensional potential surfaces using only first derivatives. *J. Chem. Phys.* **111**, 7010–7022 (1999).

86. Heyden, A., Bell, A. T. & Keil, F. J. Efficient methods for finding transition states in chemical reactions: Comparison of improved dimer method and partitioned rational function optimization method. *J. Chem. Phys.* **123**, 224101:224101–224101:224114 (2005).

87. Ahlrichs, R., Bar, M., Haser, M., Horn, H. & Kolmel, C. Electronic-Structure Calculations on Workstation Computers - the Program System Turbomole. *Chem. Phys. Lett.* **162**, 165–169 (1989).

88. Treutler, O. & Ahlrichs, R. Efficient Molecular Numerical-Integration Schemes. *J. Chem. Phys.* **102**, 346–354 (1995).

89. Von Arnim, M. & Ahlrichs, R. Performance of parallel TURBOMOLE for density functional calculations. *J. Comput Chem.* **19**, 1746–1757 (1998).

90. Schafer, A., Horn, H. & Ahlrichs, R. Fully Optimized Contracted Gaussian-Basis Sets for Atoms Li to Kr. *J. Chem. Phys.* **97**, 2571–2577 (1992).

91. Weigend, F. & Ahlrichs, R. Balanced basis sets of split valence, triple zeta valence and quadruple zeta valence quality for H to Rn: Design and assessment of accuracy. *Phys. Chem. Chem. Phys.* **7**, 3297–3305 (2005).

92. Russo, T. V., Martin, R. L. & Hay, P. J. Effective Core Potentials for Dft Calculations. *J. Phys. Chem.* **99**, 17085–17087 (1995).

93. Eichkorn, K., Weigend, F., Treutler, O. & Ahlrichs, R. Auxiliary basis sets for main row atoms and transition metals and their use to approximate Coulomb potentials. *Theor. Chem. Acc.* **97**, 119–124 (1997).

94. Weigend, F. Accurate Coulomb-fitting basis sets for H to Rn. *Phys. Chem. Chem. Phys.* **8**, 1057–1065 (2006).

95. Todorov, I. T., Smith, W., Trachenko, K. & Dove, M. T. DL_POLY_3: new dimensions in molecular dynamics simulations via massive parallelism. *J. Mater. Chem.* **16**, 1911–1918 (2006).

96. Jorgensen, W. L., Chandrasekhar, J., Madura, J. D., Impey, R. W. & Klein, M. L. Comparison of Simple Potential Functions for Simulating Liquid Water. *J. Chem. Phys.* **79**, 926–935 (1983).

97. Andersen, H. C. Rattle - a Velocity Version of the Shake Algorithm for Molecular-Dynamics Calculations. *J. Comput Phys.* **52**, 24–34 (1983).

98. Smith, W. & Forester, T. R. Parallel Macromolecular Simulations and the Replicated Data Strategy .2. The Rd-Shake Algorithm. *Comput. Phys. Commun.* **79**, 63–77 (1994).

99. Swope, W. C., Andersen, H. C., Berens, P. H. & Wilson, K. R. A Computer-Simulation Method for the Calculation of Equilibrium-Constants for the Formation of Physical Clusters of Molecules - Application to Small Water Clusters. *J. Chem. Phys.* **76**, 637–649 (1982).

100. Jorgensen, W. L. Optimized Intermolecular Potential Functions for Liquid Alcohols. *J. Phys. Chem.* **90**, 1276–1284 (1986).

101. Geerke, D. P., Van & Gunsteren, W. F. The performance of non-polarizable and polarizable force-field parameter sets for ethylene glycol in molecular dynamics simulations of the pure liquid and its aqueous mixtures. *Mol. Phys.* **105**, 1861–1881 (2007).

102. Freindorf, M., Shao, Y., Furlani, T. R. & Kong, J. Lennard–Jones parameters for the combined QM/MM method using the B3LYP/6-31G*/AMBER potential. *J. Comput. Chem.* **26**, 1270–1278 (2005).

103. Heinz, H., Vaia, R. A., Farmer, B. L. & Naik, R. R. Accurate Simulation of Surfaces and Interfaces of Face-Centered Cubic Metals Using 12-6 and 9-6 Lennard-Jones Potentials. *J. Phys. Chem. C* **112**, 17281–17290 (2008).

104. Burow, A. M., Sierka, M., Dobler, J. & Sauer, J. Point defects in CaF2 and CeO2 investigated by the periodic electrostatic embedded cluster method. *J. Chem. Phys.* **130**, 174710:174711–174710:174711 (2009).

105. Nose, S. A Unified Formulation of the Constant Temperature Molecular-Dynamics Methods. *J. Chem. Phys.* **81**, 511–519 (1984).

106. Hoover, W. G. Canonical Dynamics - Equilibrium Phase-Space Distributions. *Phys. Rev. A* **31**, 1695–1697 (1985).

107. Essmann, U. et al. A Smooth Particle Mesh Ewald Method. *J. Chem. Phys.* **103**, 8577–8593 (1995).

108. Zwanzig, R. W. High-Temperature Equation of State by a Perturbation Method .1. Nonpolar Gases. *J. Chem. Phys.* **22**, 1420–1426 (1954).

109. Archontis, G., Simonson, T., Moras, D. & Karplus, M. Specific amino acid recognition by aspartyl-tRNA synthetase studied by free energy simulations. *J. Mol. Biol.* **275**, 823–846 (1998).

110. Jun, Z., Thomas, S., Masha, F. & Hiroshi, M. R. TH. Protein-protein recognition: An experimental and computational study of the R89K mutation in Raf and its effect on Ras binding. *Protein Sci.* **8**, 50–64 (1999).

111. Best, S. A., Merz, K. M. & Reynolds, C. H. Free energy perturbation study of octanol/water partition coefficients: Comparison with continuum GB/SA calculations. *J. Phys. Chem. B* **103**, 714–726 (1999).

112. Shirts, M. R. & Pande, V. S. Comparison of efficiency and bias of free energies computed by exponential averaging, the Bennett acceptance ratio, and thermodynamic integration. *J. Chem. Phys.* **122**, 144107:144101–144107:144116 (2005).

113. Lu, N. D., Singh, J. K. & Kofke, D. A. Appropriate methods to combine forward and reverse free-energy perturbation averages. *J. Chem. Phys.* **118**, 2977–2984 (2003).

114. Ryde, U. How Many Conformations Need To Be Sampled To Obtain Converged QM/MM Energies? The Curse of Exponential Averaging. *J. Chem. Theory Comput.* **13**, 5745–5752 (2017).

115. Bennett, C. Efficient Estimation of Free Energy Differences from Monte Carlo Data. *J. Comput Phys.* **22**, 245–268 (1976).

116. Shirts, M. R., Bair, E., Hooker, G. & Pande, V. S. Equilibrium free energies from nonequilibrium measurements using maximum-likelihood methods. *Phys. Rev. Lett.* **91**, 140601 (2003).

117. Kreyszig, E. *Advanced Engineering Mathematics* 9th edn. (John Wiley & Sons, Inc., 2006).

118. Klamt, A., Jonas, V., Bürger, T. & Lohrenz, J. C. W. Refinement and Parametrization of COSMO-RS. *J. Phys. Chem. A* **102**, 5074–5085 (1998).

119. Klamt, A. Conductor-like Screening Model for Real Solvents: A New Approach to the Quantitative Calculation of Solvation Phenomena. *J. Phys. Chem.* **99**, 2224–2235 (1995).

120. Marsh, K. N. COSMO-RS from Quantum Chemistry to Fluid Phase Thermodynamics and Drug Design. By A. Klamt. Elsevier: Amsterdam, The Netherlands, 2005. 246 pp. $US 165. *J. Chem. Eng. Data* **51**, 1480–1480 (2006).

121. Fernandez, D. P., Goodwin, A. R. H., Lemmon, E. W., Sengers, J. M. H. L. & Williams, R. C. A formulation for the static permittivity of water and steam at temperatures from 238 K to 873 K at pressures up to 1200 MPa, including derivatives and Debye-Huckel coefficients. *J. Phys. Chem. Ref. Data* **26**, 1125–1166 (1997).

Author contributions

M.Z. did all calculations for Ni, Cu, Ag and parts of the calculations for Pd. M.S. performed all calculations for Pt and parts of the calculations for Pd. S.K.K. did all calculations for Au. A.H. conceived and supervised the project. The manuscript was written by M.Z. and A.H. with input from all the authors.

Competing interests

The authors declare no competing interests.

Additional information

Supplementary information is available for this paper at https://doi.org/10.1038/s42004-020-00428-4.

Correspondence and requests for materials should be addressed to A.H.

Reprints and permission information is available at http://www.nature.com/reprints

Publisher's note Springer Nature remains neutral with regard to jurisdictional claims in published maps and institutional affiliations.